



Thermophysical Properties of Vanadium Melts and Discussion of Thermal Diffusivity in Mott's Theory

Manabu Watanabe¹ · Masayoshi Adachi² · Hiroyuki Fukuyama¹

Received: 28 November 2023 / Accepted: 20 December 2023 / Published online: 27 February 2024
© The Author(s) 2024

Abstract

The temperature dependence of density, normal spectral emissivity, heat capacity at constant pressure, and thermal conductivity of the V melt were measured with high accuracy using electromagnetic levitation in a static magnetic field. Surface vibration, translational motion, and convection of the electromagnetically levitated droplet sample were suppressed by the magnetic field. In the measurement of thermal conductivity, convection in the V-melt was sufficiently suppressed by the application of a field of 7 T or higher. In this study, the measured emissivity and thermal conductivity are compared with those evaluated using the free-electron models (Drude model and Wiedemann–Franz rule). Correlations between the density of states and thermal diffusivity at the Fermi energy of transition metals in the liquid state are investigated and the applicability of Mott's s – d scattering model is discussed.

Keywords Density of state · Heat capacity at constant pressure · Normal spectral emissivity · Thermal conductivity

1 Introduction

Over the past 80 years, the correlation between the density of states (DOS) and physical properties such as electrical resistivity [1], Seebeck coefficient [2–4], and thermal conductivity (κ) [5] have been investigated. In 1936, Mott [6–8] reported

Selected Papers of the 22nd European Conference on Thermophysical Properties.

✉ Manabu Watanabe
watanabe.m.cb@m.titech.ac.jp

✉ Hiroyuki Fukuyama
hiroyuki.fukuyama.b6@tohoku.ac.jp

¹ Department of Materials Science and Engineering, Tokyo Institute of Technology, Yokohama 226-8502, Japan

² Institute of Multidisciplinary Research for Advanced Materials, Tohoku University, Sendai 980-8577, Japan

that the electrical resistivity for transition metals is dominated by the transition of the s -electron to the DOS of the d -state at the Fermi level that now constitutes “Mott’s s – d scattering model”. Aisaka and Shimizu [5] reported that the electrical resistivity and the Seebeck coefficient of the transition metals in a solid state can be explained using the extended Mott’s s – d scattering model. In 1986, Zinov’yev et al. [9] measured the thermal diffusivity (α) of transition metals in a liquid state using a plane temperature wave method and investigated the relationship between the thermophysical properties in a liquid state and the DOS for transition metals. However, Zinov’yev et al. did not find a linear relationship between α and the reciprocal DOS for two reasons:

- 1 The plane temperature wave method may not be valid for the thermal diffusivity measurement because of circulation flows arising from temperature gradients in the sample as pointed out by Assael et al. [10].
- 2 Zinov’yev used the DOS at 300 K to investigate the relationship between the DOS and α at the liquid state.

Our group developed a laboratory facility called PROSPECT for high accuracy measurement of thermophysical properties of matter in the liquid state, [11–22]. PROSPECT exploits an electromagnetic levitation technique (EML) and employs a static magnetic field that can suppress convection, translational motion, and surface vibrations in levitated melts. We investigated the relationship between α and reciprocal DOS for six different transition metals in 2021 [23]. We concluded that α is proportional to the reciprocal DOS at Fermi level ($(N(E_F))^{-1}$) for these six transition metals in the liquid state that can be explained by Mott’s s – d scattering model.

For vanadium melts, Zinov’yev et al. [9] measured α using the plane-temperature method, and Pottlacher et al. [24] evaluated α from the measured electric resistivity using the Wiedemann–Franz law. This law may underestimate the thermal conductivity of vanadium melts because it does not consider contributions to heat transfer from the thermal vibration of atoms. To discuss α of the V melt using the s – d scattering model, an accurate α of the V melt is required. The purpose of this study is to first measure the density (ρ), normal spectral emissivity (ϵ), heat capacity at constant pressure (C_p), and electrical resistivity (κ) to determine α of the V melt and then discuss the mechanism underlying thermal transport of transition metals in the liquid state based on Mott’s s – d scattering model.

2 Experimental

The purity of the vanadium sample was 99.9 mass%, the supplier being Rare Metallic Co. Ltd, Japan. After experiments, the oxygen contamination in the sample ranged from 0.02 mass% to 0.18 mass%, which was measured using a LECO elemental gas analyzer (ON-836, LECO, St. Joseph, USA).

The experimental details have been reported elsewhere [11, 14, 23], and therefore the procedure is only outlined here. The experimental apparatus (PROSPECT; see

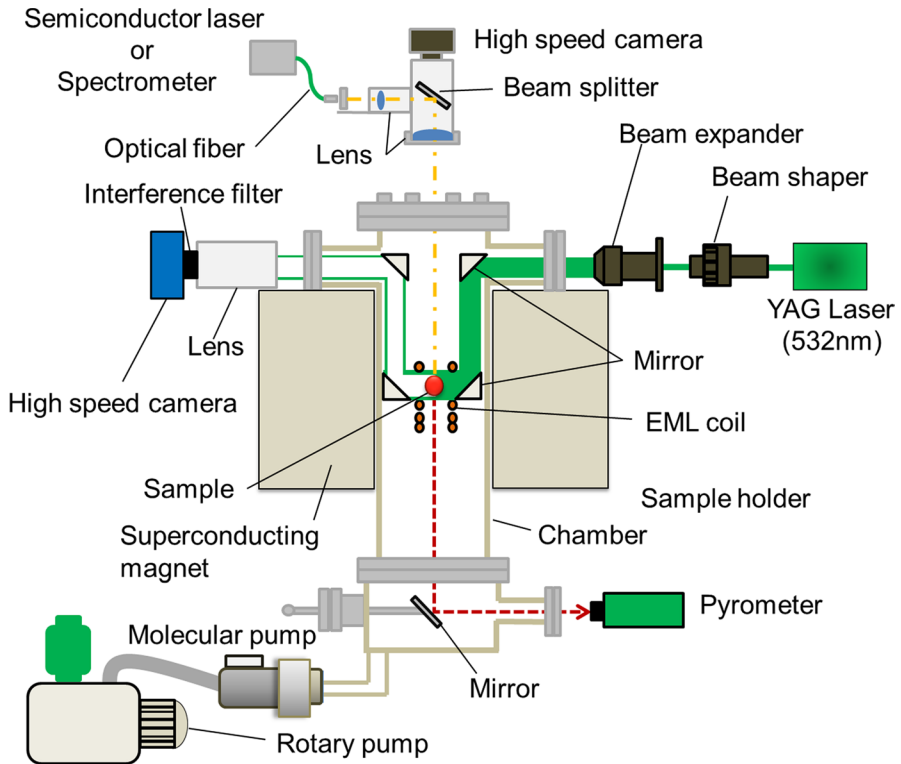


Fig. 1 Schematic of the experimental apparatus (PROSPECT)

Fig. 1) involves both a turbomolecular and a rotary pump to evacuate the chamber up to 10^{-3} Pa. After evacuation, the chamber is filled with Ar-5 vol% H_2 gas up to 0.1 MPa to avoid sample oxidation. Then, an EML coil carrying an AC current ranging from 310 A to 350 A levitates the sample while a radio-frequency generator (Easy Heat 8310, Ameritherm Inc., New York, USA) heats it. Employing a superconducting magnet (JM TD-10T 120SSFX, Japan Superconductor Technology, Kobe, Japan), a static magnetic field is applied to suppress the surface vibrations, translational motion, and convection of the levitated melt.

A single-color pyrometer (detection wavelength range: 1.45–1.8 μm , IGA140/MB25, IMPAC Pyrometer, LumaSense Technologies, Germany), which was calibrated using the sample's emissivity at melting point (2183 K), records the sample temperature [25]. In the determination of this temperature, the emissivity of the sample in the liquid state was assumed the same as that at the melting point. Helium gas is supplied to the chamber to control the sample temperature.

2.1 Density Measurement

Shadow images of the droplet, levitated electromagnetically under a static magnetic field of 4 T, were obtained from the horizontal direction using a shadowgraph optical system, consisting of a YAG laser (532 nm), a beam expander, and a high-speed camera. The frame rate of the high-speed camera was set at 150 fps and sample images were recorded for 20 s for each temperature setting. Three stainless-steel balls of different diameters (4.998 mm, 6.348 mm, and 7.000 mm) were imaged with the same optical system in converting pixels spanned into lengths.

The sample density (ρ) is defined as

$$\rho = \frac{m}{V}, \quad (1)$$

where m and V denote the sample mass and volume, respectively. The sample mass was measured before and after each density measurement to evaluate the uncertainty through sample evaporation. The sample volume was determined from average values of the calculated volumes, obtained from the shadowgraph images assuming the levitated samples were rotationally symmetric around the vertical axis.

2.2 Normal Spectral Emissivity Measurement

The normal spectral emissivity (ε) of samples, levitated under a field of 3 T, is expressed as

$$\varepsilon(\lambda, T) = \frac{E_s(\lambda, T)}{E_B(\lambda, T)}, \quad (2)$$

$$E_B(\lambda, T) = \frac{2\pi hc_0^2}{\lambda^5 \left(\exp\left(\frac{hc}{\lambda k_B T}\right) - 1 \right)}, \quad (3)$$

where $E_s(\lambda, T)$ and $E_B(\lambda, T)$ denote the normal spectral emissive power of the sample and a blackbody, respectively, λ denotes wavelength, T temperature, h Planck's constant, k_B Boltzmann's constant, and c the speed of light. $E_B(\lambda, T)$ is Planck's radiation law. $E_s(\lambda, T)$ is measured using a multichannel spectrometer (wavelength range (530–1100) nm, USB2000, Ocean Optics Inc., FL, USA) and is obtained from

$$E_s(\lambda, T) = C_0(\lambda) \cdot X(\lambda, T), \quad (4)$$

where $X(\lambda, T)$ denotes the output count of the multichannel spectrometer, measured from the top of the sample droplet, and $C_0(\lambda)$ is a coefficient of proportionality determined from the calibration of the spectrometer using a quasi-blackbody component [14].

2.3 Laser Modulation Calorimetry

In the laser modulation calorimetry method, the top of the levitated sample was heated in a periodic manner by a semiconductor laser (laser wavelength: (940 ± 20) nm, maximum power: 67.5 W, SPOLD L13920-511, Hamamatsu Photonics, Japan) with an output power $[P_0(1 + \cos\omega t)]$ and angular frequency (ω); the temperature response was then monitored at the bottom of the sample by the pyrometer.

2.3.1 Heat Capacity Measurements

The heat capacity of the V melts at constant pressures (C_p) were measured through laser modulation calorimetry. The measurement requires the temperature amplitude (ΔT_{ac}) and the phase shift ($\Delta\phi$) between the irradiated laser power and temperature response. The three quantities are expressed as

$$C_p = \frac{\alpha_N S_h A P_0}{\omega \Delta T_{ac}} f, \quad (5)$$

$$\Delta\phi = \arccos \left\{ \frac{\tau_c}{\omega} \left(\frac{1}{\tau_c \tau_r} - \omega^2 \right) f \right\}, \quad (6)$$

$$f = \left(1 + \frac{1}{\omega^2 \tau_r^2} + \omega^2 \tau_c^2 \right)^{-\frac{1}{2}}, \quad (7)$$

where α_N denotes the laser absorptivity, S_h the area ratio of the laser-irradiated part of the levitated sample, A the surface area of the levitated sample, and f a correction function; τ_r and τ_c denote the external and internal thermal relaxation times. In this study, α_N was assumed the same as ε based on Kirchhoff's law. Because τ_c decreases with increasing convective flow in the melt, the quasi-adiabatic condition (i.e., $\tau_c/\tau_r \ll 1$) is satisfied by a proper choice of laser-modulation frequency and static magnetic field. In C_p measurements, a relatively low magnetic field intensity (2.2–2.5 T) was applied to levitate the sample and maintain convective flow. The relaxation times, τ_c and τ_r , are obtained by fitting Eq. 6 to the relation between $\Delta\phi$ and the modulation frequency. After fitting, C_p is determined using Eq. 6 with the values of τ_c , τ_r , and ΔT_{ac} .

2.3.2 Thermal Conductivity Measurements

Thermal conductivity (κ) was also measured through laser modulation calorimetry. The unsteady state heat conduction equation in spherical coordinates is expressed as

$$\rho C_p \frac{\partial T}{\partial t} = \kappa \left\{ \frac{1}{r^2} \frac{\partial}{\partial r} \left(r^2 \frac{\partial T}{\partial r} \right) + \frac{1}{r^2 \sin\theta} \frac{\partial}{\partial \theta} \left(\sin\theta \frac{\partial T}{\partial \theta} \right) \right\} + Q(r, \theta), \quad (8)$$

where $Q(r, \theta)$ denotes the heat generated by induction current, t time, and r and θ denote the radial distance and polar angle, respectively, with the center of the sample as the origin. No azimuthal dependence for T and Q is assumed.

When the upper part of the droplet is irradiated by the modulated laser beam, the temperature at each point in the droplet ($T(r, \theta, t)$) increases in average temperature and the modulation amplitude from the initial temperature and then reaches a stationary modulation state with a certain constant average temperature and amplitude. In this stationary modulation state, $T(r, \theta, t)$ is expressed as

$$T(r, \theta, t) = T_0 + \Delta T_{av}(r, \theta) + \Delta T_{ac}(r, \theta, t), \quad (9)$$

where T_0 denotes the initial temperature of the droplet, $\Delta T_{av}(r, \theta)$ the increase in average temperature, and ΔT_{ac} takes the form

$$\Delta T_{ac}(r, \theta, t) = \Delta T_{ac}^{in}(r, \theta)\cos\omega t + \Delta T_{ac}^{out}(r, \theta)\sin\omega t, \quad (10)$$

where $\Delta T_{ac}^{in}(r, \theta)$ and $\Delta T_{ac}^{out}(r, \theta)$ denote the in-phase and out-of-phase components of $\Delta T_{ac}(r, \theta, t)$. On substituting Eqs. 9 and 10 into Eq. 8, a steady-state system of linear equations for $\Delta T_{ac}^{in}(r, \theta)$ and $\Delta T_{ac}^{out}(r, \theta)$ are obtained

$$\rho C_p \omega \Delta T_{ac}^{out} = \kappa \left\{ \frac{1}{r^2} \frac{\partial}{\partial r} \left(r^2 \frac{\partial(\Delta T_{ac}^{in})}{\partial r} \right) + \frac{1}{r^2 \sin\theta} \frac{\partial}{\partial \theta} \left(\sin\theta \frac{\partial(\Delta T_{ac}^{in})}{\partial \theta} \right) \right\}, \quad (11)$$

$$\rho C_p \omega (-\Delta T_{ac}^{in}) = \kappa \left\{ \frac{1}{r^2} \frac{\partial}{\partial r} \left(r^2 \frac{\partial(\Delta T_{ac}^{out})}{\partial r} \right) + \frac{1}{r^2 \sin\theta} \frac{\partial}{\partial \theta} \left(\sin\theta \frac{\partial(\Delta T_{ac}^{out})}{\partial \theta} \right) \right\}. \quad (12)$$

Equations 11 and 12 were solved using the finite element method with boundary conditions at the laser-irradiated and non-laser-irradiated droplet surfaces to obtain the $\Delta T_{ac}^{in}(r, \theta)$ and $\Delta T_{ac}^{out}(r, \theta)$ distributions in the droplet. Using the values obtained, the phase shift $\Delta\phi$ is given by

$$\Delta\phi = \tan^{-1} \left(\frac{\Delta T_{ac}^{out}}{\Delta T_{ac}^{in}} \right). \quad (13)$$

The unknown parameter, κ , is obtained by fitting the modulation frequency dependence of the phase shift obtained from the above analysis to the experimentally obtained phase shift using the least-squares method.

3 Results

3.1 Density

Figure 2 and Table 1 present results of the temperature dependence of the ρ of V melt with values obtained from the literature [26–31]. Our results show clear linearity over a range that includes the supercooled temperature region and are in

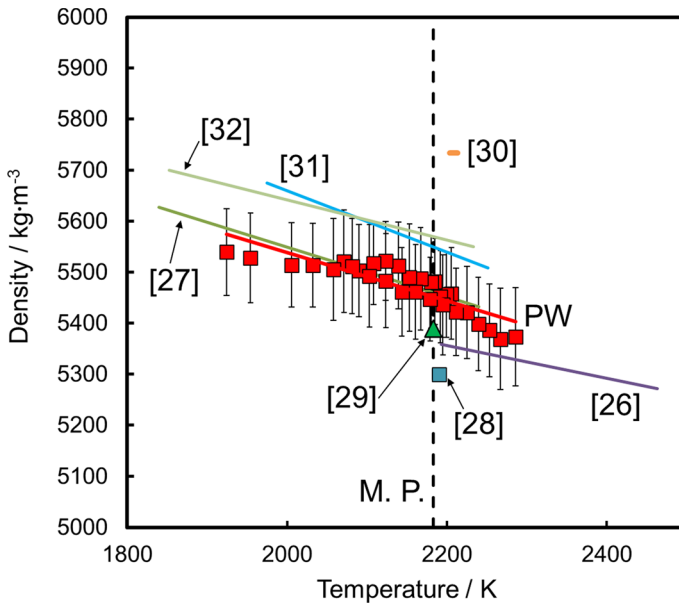


Fig. 2 Temperature dependence of density of vanadium melt. Black-dashed line marks the melting point (M.P.). Error bars show the expanded uncertainty ($k=2$). PW: Present work (EML with a static magnetic field), [26]: Saito et al. (EML), [27]: Paradis et al. (ESL), [28]: Elyutin and Kostikov (Pendant drop), [29]: Ivaschenko and Marcgenuk (Pendant drop), [30]: Maurakh (Maximum bubble pressure), [31]: Reiplinger and Brillo (EML), [32]: Zhang et al. (ESL)

good agreement with literature data reported by Saito et al. [26], Paradis et al. [27], Ivaschenko and Marcgenuk [29], Reiplinger and Brillo [31], and Zhang et al. [32]. The density ρ can be expressed as

$$\rho = \rho_c (T - T_m) + \rho_m, \quad (14)$$

where ρ_c denotes the coefficient of proportionality between density and temperature, T_m the melting point, and ρ_m the density at the melting point. The error bar shows the expanded uncertainty ($k=2$), which is described in Sect. 4.1.1.

In determining the volume from the side-view image taken in the pendant drop method, Elyutin et al. [28] assumed that the melt has a symmetrical shape, and gave an uncertainty in calculating the volume ranging from 3 % to 5 %. This uncertainty mainly occurs in the deformation of drops from the axial symmetry in the vertical direction. Because of the large uncertainty, the present work differs from the values reported by Elyutin et al. [28].

Maurakh [30] used a beryllium oxide crucible and capillary for density measurements, and there is concern that the vanadium melt sample was contaminated with oxygen or beryllium during the experiment.

Table 1 Densities of vanadium melts as functions of temperature

Reference	Temperature range/K	Method	Melting point: $(T_m)/K$	Density at T_m : $(\rho_m)/kg \cdot m^{-3}$	Temperature coefficient of density: $(\rho_c)/kg \cdot m^{-3} \cdot K^{-1}$
Present work	1924 to 2286	EML with static magnetic field	2183 [25]	5452 ± 4.86	-0.473 ± 0.05
Saito et al. [26]	2193 to 2463	EML	2181	5362	-0.320
Paradis et al. [27]	1840 to 2240	Electrostatic levitation	2183	5460	-0.49
Elyutin and Kostikov [28]	2183	Pendant drop	2183	5300	-
Ivaschenko and Marchenuk [29]	2183	Pendant drop	2183	5390	-
Maurakh [30]	2203 to 2213	Maximum bubble pressure	2183	5734 (at 2203 to 2213 K)	No temperature dependence
Reiplinger and Brillo [31]	1975 to 2251	EML	2183	5550	-0.601
Zhang et al. [32]	1853 to 2233	Electrostatic levitation	2183	5570	-0.395

3.2 Normal Spectral Emissivity

Figure 3 shows the temperature dependence of the normal spectral emissivity at 807 nm and 940 nm of V melt. The error bars show the expanded uncertainty, which is discussed in Sect. 4.1.2. The normal spectral emissivity of the V melt exhibits a negligible temperature dependence. Figure 4 and Table 2 show the wavelength dependence of the normal spectral emissivity at the melting point along with reported values [24, 33–38]. The calculated value obtained by the Drude model is also presented in Fig. 4 and is described in Sect. 4.2. The present results are in good

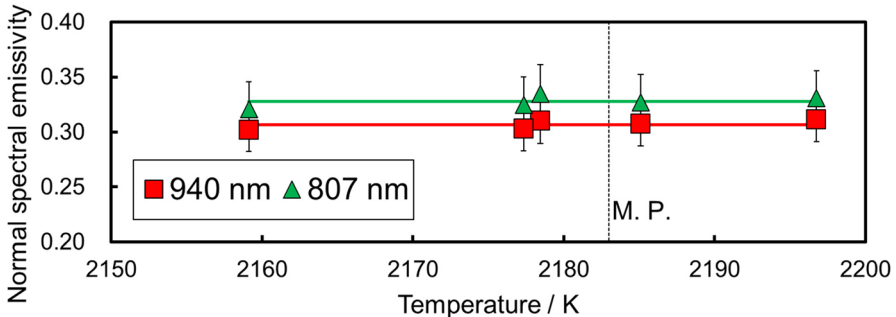


Fig. 3 Temperature dependence of normal spectral emissivity of vanadium melts at 807 and 940 nm. Black dashed line marks the melting point (M.P.). Error bars show the expanded uncertainty ($k=2$)

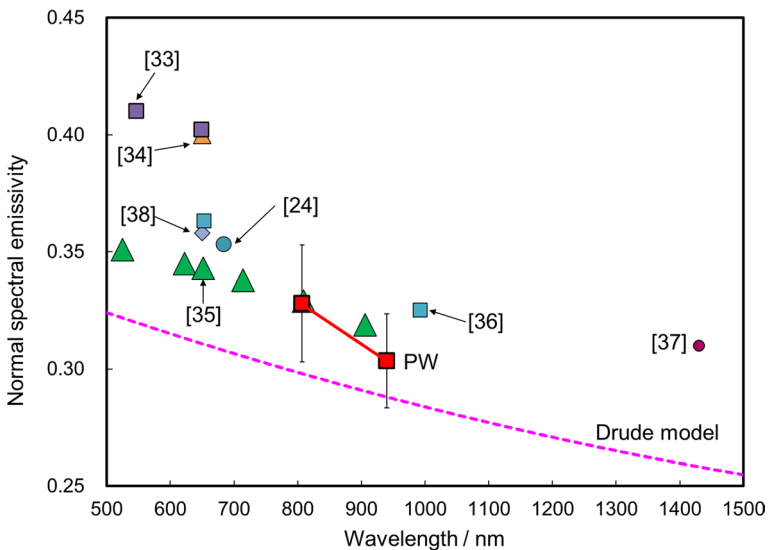


Fig. 4 Wavelength dependence of normal spectral emissivity of vanadium at melting point. The dotted line shows the values obtained from the Drude model. Error bars show the expanded uncertainty ($k=2$). PW: Present work, [24]: Pottlacher et al. (Pulse-heating with polarimeter), [33]: Lin and Froberg. (Electrostatic levitation with spectrometer), [34]: Treverton and Margrave (EML with pyrometer), [35]: McClure and Cezairliyan (Pulse-heating with pyrometer), [36]: Cezairliyan et al. (Pulse-heating with pyrometer), [37]: Ronchi et al. (Pulsed laser with pyrometer), [38]: Berezin et al. (EML with pyrometer)

Table 2 Normal spectral emissivity of vanadium melts

Reference	Method	Temperature/K	Wavelength, λ /nm	Normal spectral emissivity, ϵ
Present work	EML with spectrometer	2159–2197	807	0.328 ± 0.002
			940	0.307 ± 0.002
Pottlacher et al. [24]	Pulse-heating with polarimeter	2199	684.5	0.353
Lin and Frohberg [33]	EML with pyrometer	2202	547	0.410
			650	0.402
Treverton and Margrave [34]	EML with pyrometer	2175	650	0.400
McClure and Cezairliyan [35]	Pulse-heating with pyrometer	2201	525	0.351
			622	0.345
			652	0.343
			714	0.338
			809	0.329
Cezairliyan et al. [36]	Pulse-heating with pyrometer	2193	906	0.319
			653	0.363
			993	0.325
Ronchi et al. [37]	Pulsed laser with pyrometer	2200	1430	0.31
Berezin et al. [38]	EML with pyrometer	2193	650	0.358

agreement with the results reported by McClure and Cezairliyan [35]. The emissivity of V melts decreases with increasing wavelength.

3.3 Heat Capacity at Constant Pressure

As an example, the temperature response of the V melt to laser irradiation during the modulation calorimetry at a static magnetic field of 2.5 T and a modulation frequency of 0.08 Hz is shown in Fig. 5. Figure 6 plots $\Delta\phi$ and $\omega\Delta T_{ac}$ of the melt as a function of the modulation frequency in a static magnetic field of 2.5 T at 2016 K. The τ_r and τ_c values were obtained by curve fitting using Eq. 6 to the phase shift to be 0.32 s and 5.59 s, respectively. The value for f is 0.95 at 0.12 Hz, where the quasi-adiabatic condition ($\omega^2\tau_r^2 \gg 1 \gg \omega^2\tau_c^2$, i.e., $f \approx 1$) is satisfied. The C_p was determined using Eq. 6 employing the maximum value of $\omega\Delta T_{ac}$. Figure 7 and Table 3 present the temperature dependence of C_p for the V melt along with reported values [24, 27, 33, 34, 38, 39, 41–49]. The error bars indicate the expanded uncertainty ($k=2$), which is described at Sect. 4.1.3. The temperature dependence of C_p obtained in the present work was negligible with the range in temperature including the undercooled region. Within the expanded uncertainty, this result is in good agreement with almost all reported values except that of Hultgren et al. [46, 47], which did not

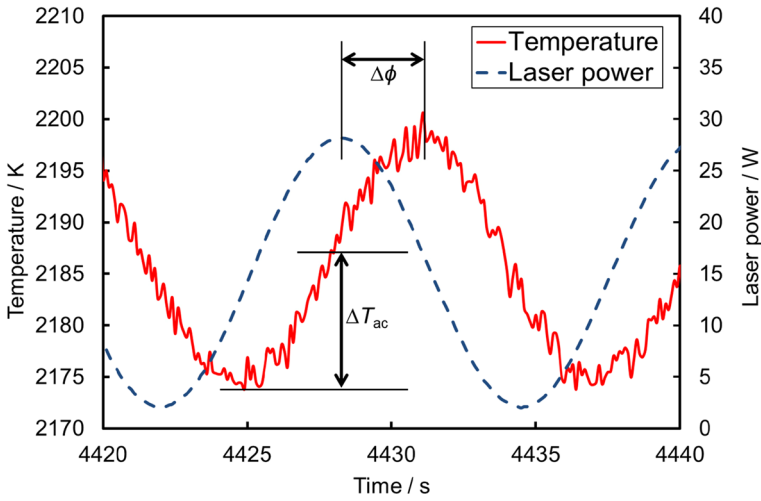


Fig. 5 Laser power (right-hand ordinate) and temperature response (left-hand ordinate) of vanadium melt during laser-modulated calorimetry with a modulation frequency at 0.08 Hz under static magnetic field of 2.5 T

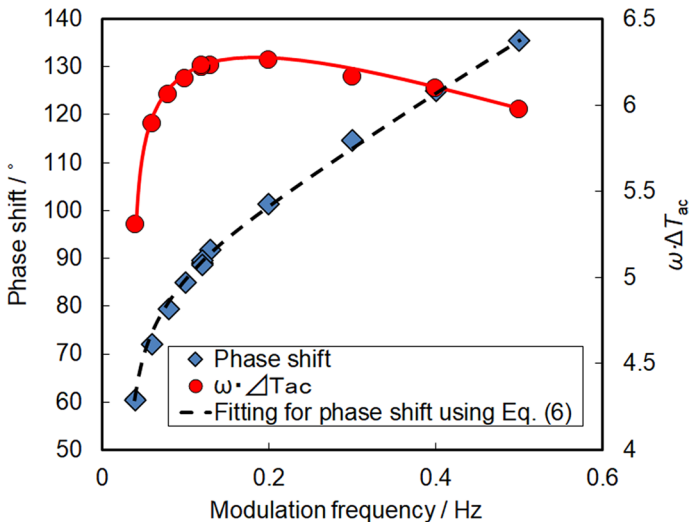


Fig. 6 Phase shift (right-hand ordinate) and $\omega\Delta T_{ac}$ (left-hand ordinate) of vanadium melt as a function of modulation frequency at 2016 K under 2.5 T

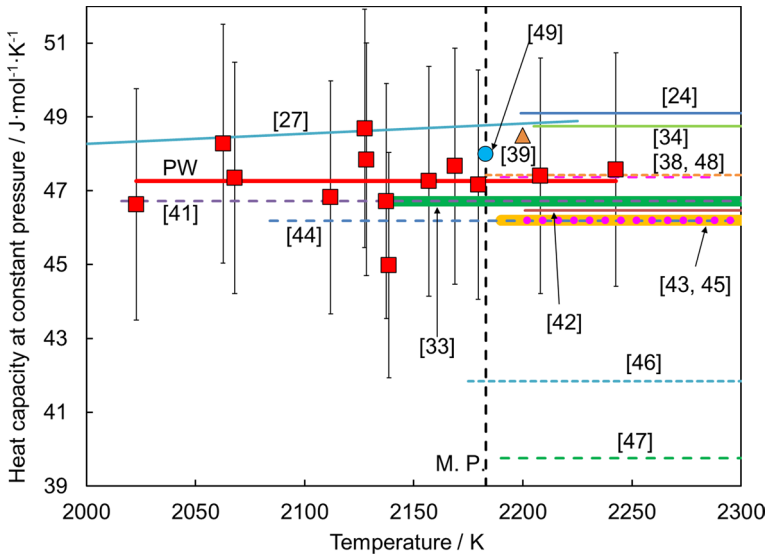


Fig. 7 Temperature dependence of heat capacity at constant pressure of vanadium melt. Dashed black line marks the melting point (M.P.). Error bars show expanded uncertainty ($k=2$). PW: Present work, [24]: Pottlacher et al. (Pulse-heating), [27]: Paradis et al. (Electrostatic levitation), [33]: Lin and Froberg (EML with drop calorimetry), [34]: Treverton and Margrave (EML with drop calorimetry), [38] Berezin et al. (EML with drop calorimetry), [39]: Ishikawa et al. (Electrostatic levitation), [41]: Schaeffers et al. (EML with drop calorimetry), [42]: Arblaster (Recommended value), [43]: NIST-JANAF (Recommended value), [44]: Berezin (EML with drop calorimetry), [45]: Desai (Recommended value), [46]: Hultgren et al. (Recommended value), [47]: Hultgren et al. (Recommended value), [48]: Dinsdale (Calculation), [49]: Sun et al. (Aerodynamic levitation)

describe details of the determination of recommended value of C_p . In consequence, a discussion on differences between their work and ours is not possible.

3.4 Thermal Conductivity

3.4.1 Effect of Static Magnetic Field on Apparent Thermal Conductivity

Because heat is carried by convective flows, the effect of applying a static magnetic field to suppress the convection in the κ measurement was investigated. Figure 8 shows the relationship between the phase shift ($\Delta\phi$) and the modulation frequency at 2167 K under a 10 T field. The value of κ was determined by reproducing the experimentally obtained relationships using Eq. 13. Figure 9 shows the static magnetic field dependence of the apparent κ of the V melt at 2183 K. The apparent κ of V melts decreased with increasing static magnetic field and converged above 7 T. This result indicates that convective flow in sample melts was sufficiently suppressed to enable thermal conductivity measurements above 7 T. From this result, thermal conductivity measurements were conducted under static magnetic fields of 10 T.

Table 3 Heat capacity at constant pressure of vanadium melts

References	Method	Temperature range, T/K	Heat capacity at constant pressure, $C_p/J\text{-mol}^{-1}\text{-K}^{-1}$
Present work	EML with Laser modulation calorimetry	2023–2243	47.26 ± 0.25
Pottlacher et al. [24]	Pulse-heating	2199–2900	49.11
Paradis et al. [27]	Electrostatic levitation	1825–2225	$0.00275 \cdot (T - 2183) + 48.78$
Ishikawa et al. [39]	Electrostatic levitation	2200	48.5
Lin and Froberg [33]	EML with drop calorimetry	2140–2632	46.72
Treverton and Margrave [34]	EML with drop calorimetry	2205–2638	48.75
Berezin et al. [38]	EML with drop calorimetry	2190–2290	47.37
Schaeffers et al. [41]	EML with drop calorimetry	2016–2403	46.72
Berezin [44]	EML with drop calorimetry	2084–2325	46.19
Sun et al. [49]	Aerodynamic levitation	2183	48.0
Arblaster [42]	Recommended value	2201–3700	46.471
NIST-JANAF [43]	Recommended value	2190–3690	46.204
Desai [45]	Recommended values	2202–3800	46.200
Hultgren et al. [46]	Recommend values	2175–3800	41.84
Hultgren et al. [47]	Recommended values	2190–3800	39.75
Dinsdale [48]	Calculation	2183–4000	47.43

Fig. 8 Phase shift of vanadium melt as a function of modulation frequency at 2167 K and 10 T

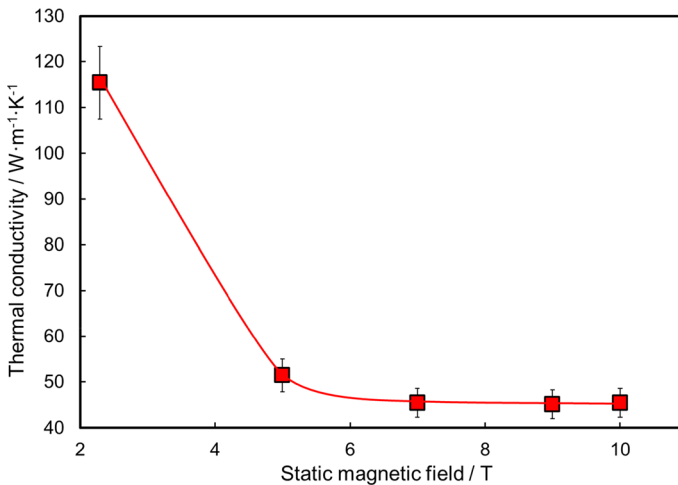
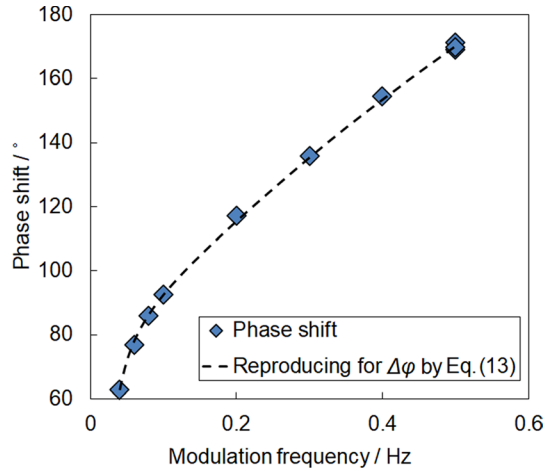


Fig. 9 Static magnetic field dependence of thermal conductivity of vanadium melts at 2183 K. The error bars show expanded uncertainty ($k=2$)

3.4.2 Thermal Conductivity and Thermal Diffusivity

Figure 10 and Table 4 show the temperature dependence of the thermal conductivity (κ) of the V melt measured in this study along with reported values [9, 24, 50, 51]. The present work shows κ increasing linearly with increasing temperature, even in the undercooled region. The error bars in Fig. 10 indicate the expanded uncertainty

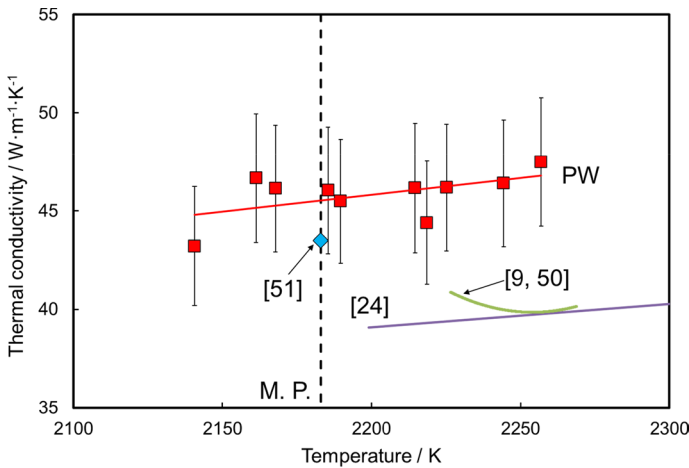


Fig. 10 Temperature dependence of thermal conductivity of vanadium melt. The dashed black line marks the melting point (M.P.). The error bars show expanded uncertainty ($k=2$). PW: Present work, [9, 50]; Zinov'yev et al. (Plane temperature wave method), [24]; Pottlacher et al. (Wiedemann–Franz law), [51] Mills et al. (Recommended value)

Table 4 Thermal conductivity of vanadium melt

Reference	Method	Temperature range, T/K	Thermal conductivity, $\kappa/W\cdot m^{-1}\cdot K^{-1}$
Present work	Laser modulation calorimetry	2141–2257	$(0.017 \pm 0.010) \times (T - 2183) + (45.5 \pm 0.38)$
Zinov'yev et al. [9, 50]	Plane temperature wave	2237–2269	$0.0014 \cdot T^2 - 6.12 \cdot T + 6939$
Pottlacher et al. [24]	Wiedemann–Franz law	2199–2900	$(-3.559 \times 10^{-6}) \cdot T^2 + 0.030 \cdot T - 9.680$
Mills et al. [51]	Recommended values	2183	43.5

($k=2$), as described in Sect. 4.1.4. Within the experimental uncertainty, the present data of κ agrees with the values reported by Mills et al. [51].

Figure 11 shows the temperature dependence of the thermal diffusivity (α), which was obtained using

$$\alpha = \frac{\kappa}{C_p \cdot \rho}. \tag{15}$$

Zinov'yev et al. [9, 50] measured α employing the plane temperature wave method; their value of α was higher than the present data. As described in Sect. 1, Assael et al. [10] reported a higher value of α than the true values obtained using the plane temperature wave method because of the circulatory flow. In contrast, the value of κ reported by Zinov'yev et al. was lower than the present data but they had used the low C_p value of Hultgren et al. [47].

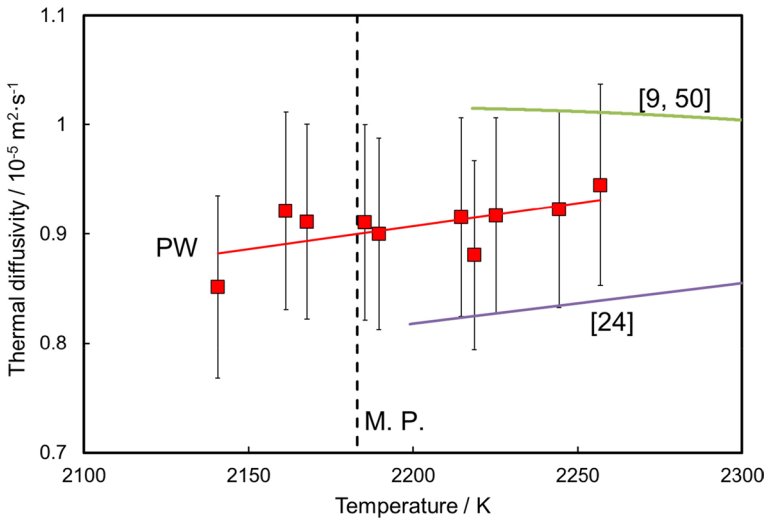


Fig. 11 Temperature dependence of thermal diffusivity of vanadium melt. The dashed black line marks the melting point (M.P.). The error bars show expanded uncertainty ($k=2$). PW: Present work, [9, 50]; Zinov'yeu et al. (Plane temperature wave method), [24]; Pottlacher et al. (Wiedemann–Franz law)

The present work on κ and α gave higher values than the data reported in Pottlacher et al. [24], in which α and κ were determined using the Wiedemann–Franz law and the electric conductivity to be discussed in Sect. 4.3.

4 Discussion

4.1 Uncertainty Analysis

The uncertainty associated with measurements was evaluated based on the Guide to the Expression of Uncertainty in Measurement (GUM) [52]. In addition, the regression analysis was conducted to evaluate the experimental variance of the slope and intercept in the equations.

4.1.1 Uncertainty Analysis of the Density Measurement

The uncertainty in the density measurement was evaluated using

$$u^2(\rho) = \left(\frac{\partial \rho}{\partial V} \right)^2 u^2(V) + \left(\frac{\partial \rho}{\partial M} \right)^2 u^2(M), \quad (16)$$

where $u(\rho)$ denotes the combined standard uncertainty in the density measurement, $u(V)$ the uncertainty from the standard deviation of values of volume evaluated from 3000 droplet images, and $u(M)$ the uncertainty of mass due to sample evaporation. By way of example, the uncertainty of density measurement at 2153 K is outlined in Table 5. The dominant component of the uncertainty is $u(V)$, and the value of $U=2u(\rho)$ was $105 \text{ kg}\cdot\text{m}^{-3}$, which corresponds to 1.9 % of the density value ($5490 \text{ kg}\cdot\text{m}^{-3}$). For all density measurements, U is between 1.4 % and 1.9 %.

4.1.2 Uncertainty Analysis of Normal Spectral Emissivity Measurement

Similarly, the uncertainty of the normal spectral emissivity is expressed as

$$u^2(\epsilon) = \left(\frac{\partial \epsilon}{\partial C_0} \right)^2 u^2(C_0) + \left(\frac{\partial \epsilon}{\partial T} \right)^2 u^2(T_{\text{Pyro}}) + \left(\frac{\partial \epsilon}{\partial T} \right)^2 u^2(T_{\text{Cal}}), \quad (17)$$

where $u(\epsilon)$ denotes the combined standard uncertainty of the normal spectral emissivity; $u(C_0)$, $u(T_{\text{Pyro}})$, and $u(T_{\text{Cal}})$ denote respectively the standard uncertainty of the coefficient of C_0 , the accuracy of the pyrometer, and the uncertainty of the pyrometer calibration using the temperature profile at the melting point. Based on the pyrometer specifications, $u(T_{\text{Pyro}})$ was evaluated as 0.3 % of the measured value plus 1 K up to 1773 K and 0.5 % of the measured value above 1773 K.

As an example, the uncertainty evaluation of the emissivity at 940 nm for V melts at 2177 K is outlined in Table 6. The dominant contribution to $u(\epsilon)$ is $u(T_{\text{Cal}})$. The expanded uncertainty $U=2u(\epsilon)$ is 0.020, which corresponds to 6.6 % of the emissivity. For the V melts overall, the expanded uncertainty varies from 7.6 % to 7.7 % at 807 nm, and from 6.5 % to 6.6 % at 940 nm, respectively.

4.1.3 Uncertainty Analysis of Heat Capacity Measurement

The uncertainty of the heat capacity is given by

$$u^2(C_p) = \left(\frac{\partial C_p}{\partial \epsilon} \right)^2 u^2(\epsilon) + \left(\frac{\partial C_p}{\partial \Delta T_{\text{ac}}} \right)^2 u^2(\Delta T_{\text{ac}}) + \left(\frac{\partial C_p}{\partial m} \right)^2 u^2(m), \quad (18)$$

where $u(C_p)$ denotes the combined standard uncertainty of the heat capacity; $u(\epsilon)$, $u(\Delta T_{\text{ac}})$, and $u(m)$ denote respectively the uncertainties of the normal spectral emissivity, temperature amplitude, and sample mass. As an example, Table 7 outlines the evaluation of the uncertainty in heat capacity measurements of the V melt at 2137 K. The factor $u(\epsilon)$ contributes strongly to $u(C_p)$ with an expanded uncertainty $U=2u(C_p)$ of $3.18 \text{ J}\cdot\text{mol}^{-1}\cdot\text{K}^{-1}$, which corresponds to 6.8 % of the heat capacity. For the V melts overall, the expanded uncertainty for all measurements ranged from 6.6 % to 6.8 %, respectively.

Table 5 Uncertainty evaluation in density measurements at 2153 K

Component	Standard uncertainty	Sensitivity coefficient	Contribution
Uncertainty of volume: $u(V)$	$1.09 \times 10^{-9} \text{ m}^3$	$\frac{\partial \rho}{\partial V} = -4.70 \times 10^{10} \text{ kg} \cdot \text{m}^{-6}$	$-51.5 \text{ kg} \cdot \text{m}^{-3}$
Uncertainty of mass loss due to evaporation: $u(M)$	$1.34 \times 10^{-6} \text{ kg}$	$\frac{\partial \rho}{\partial M} = 8.56 \times 10^6 \text{ m}^{-3}$	$11.5 \text{ kg} \cdot \text{m}^{-3}$
Combined standard uncertainty $u(\rho)$			$52.7 \text{ kg} \cdot \text{m}^{-3}$
Expanded uncertainty $U = 2u(\rho)$ (95.45 % confidence)			$105 \text{ kg} \cdot \text{m}^{-3}$

$\rho = 5490 \text{ kg} \cdot \text{m}^{-3}$ at 2153 K

Table 6 Uncertainty evaluation in emissivity measurement at 940 nm at 2177 K

Component	Standard uncertainty	Sensitivity coefficient	Contribution
Uncertainty of coefficient: $u(C_0)$	$0.002 \text{ W}\cdot\text{m}^{-2}\cdot\mu\text{m}^{-1}$	$\frac{\partial \varepsilon}{\partial C_0} = 0.30 \text{ W}^{-1}\cdot\text{m}^2\cdot\mu\text{m}$	0.001
Accuracy of pyrometer: $u(T_{\text{pyro}})$	5.43 K	$\frac{\partial \varepsilon}{\partial T} = -9.85 \times 10^{-4}\cdot\text{K}^{-1}$	-0.005
Uncertainty of pyrometer calibration at liquids temperature: $u(T_{\text{cal}})$	8.58 K	$\frac{\partial \varepsilon}{\partial T} = -9.85 \times 10^{-4}\cdot\text{K}^{-1}$	-0.008
Combined standard uncertainty $u(\varepsilon)$			0.010
Expanded uncertainty $U = 2u(\varepsilon)$			0.020

$\varepsilon = 0.30$ at 2177 K

4.1.4 Uncertainty Analysis of Thermal Conductivity Measurement

The uncertainty of the thermal conductivity was evaluated by the following equation:

$$u(\kappa)^2 = \left(\frac{\partial \kappa}{\partial \Delta \phi} \right)^2 u^2(\Delta \phi) + \left(\frac{\partial \kappa}{\partial \rho} \right)^2 u^2(\rho) + \left(\frac{\partial \kappa}{\partial C_p} \right)^2 u^2(C_p), \quad (19)$$

where $u(\kappa)$ denotes the combined standard uncertainty of the thermal conductivity, and $u(\Delta \phi)$ the uncertainty of the phase shift, which was evaluated as the standard deviation of the phase shift at 0.5 Hz corresponding to the highest frequency. As an example, Table 8 lists the uncertainty contributions in the thermal conductivity measurement $u(\kappa)$ of the V melt at 2215 K. The dominant contribution is $u(C_p)$ with an expanded uncertainty $U = 2u(\kappa)$ of $3.30 \text{ W}\cdot\text{m}^{-1}\cdot\text{K}^{-1}$, which corresponds to 7.1 % of the thermal conductivity. The expanded uncertainty for all measurements of the V melts ranged from 6.9 % to 7.1 %, respectively.

4.1.5 Uncertainty analysis of Thermal Diffusivity

$$u(\alpha)^2 = \left(\frac{\partial \alpha}{\partial \kappa} \right)^2 u^2(\kappa) + \left(\frac{\partial \alpha}{\partial \rho} \right)^2 u^2(\rho) + \left(\frac{\partial \alpha}{\partial C_p} \right)^2 u^2(C_p), \quad (20)$$

where $u(\alpha)$ denotes the combined standard uncertainty of the thermal diffusivity. As an example, Table 9 lists the uncertainty contributions in the thermal conductivity $u(\alpha)$ of the V melt at 2215 K. The dominant contribution is $u(\kappa)$ with an expanded uncertainty $U = 2u(\alpha)$ of $9.08 \times 10^{-7} \text{ m}^2\cdot\text{s}^{-1}$, which corresponds to 9.9 % of the thermal diffusivity. The expanded uncertainty for all measurements of the V melts ranged from 9.7 % to 9.9 %, respectively.

4.2 Drude Model

As indicated by the dashed line in Fig. 4, ε was calculated using the Drude model. The Drude model had been previously described in Ref. [22] and is only outlined here. The values used in this study are listed in Table 10. Given the number of valence electrons, the number of free electrons per atom reported

Table 7 Uncertainty evaluation in heat capacity at constant pressure at 2137 K

Component	Standard uncertainty	Sensitivity coefficient	Contribution
Uncertainty of normal spectral emissivity: $u(\epsilon)$	0.010	$\frac{\partial C_p}{\partial \epsilon} = 2987 \text{ J}\cdot\text{kg}^{-1}\cdot\text{K}^{-1}$	$30.1 \text{ J}\cdot\text{kg}^{-1}\cdot\text{K}^{-1}$
Uncertainty of temperature amplitude: $u(\Delta T_{\text{ac}})$	0.044 K	$\frac{\partial C_p}{\partial \Delta T_{\text{ac}}} = -190 \text{ J}\cdot\text{kg}^{-1}\cdot\text{K}^{-2}$	$-8.34 \text{ J}\cdot\text{kg}^{-1}\cdot\text{K}^{-1}$
Uncertainty of mass: $u(m)$	$6.00 \times 10^{-8} \text{ kg}$	$\frac{\partial C_p}{\partial m} = 135 \times 10^6 \text{ J}\cdot\text{kg}^{-2}\cdot\text{K}^{-1}$	$0.08 \text{ J}\cdot\text{kg}^{-1}\cdot\text{K}^{-1}$
Combined standard uncertainty $u(C_p)$			$31.2 \text{ J}\cdot\text{kg}^{-1}\cdot\text{K}^{-1}$
Expanded uncertainty $U = 2u(C_p)$			$62.5 \text{ J}\cdot\text{kg}^{-1}\cdot\text{K}^{-1}$ ($= 3.18 \text{ J}\cdot\text{mol}^{-1}\cdot\text{K}^{-1}$)

$C_p = 46.7 \text{ J}\cdot\text{mol}^{-1}\cdot\text{K}^{-1}$ at 2137 K

Table 8 Uncertainty evaluation in thermal conductivity measurement at 2215 K

Component	Standard uncertainty	Sensitivity coefficient	Contribution (W·m ⁻¹ ·K ⁻¹)
Uncertainty of function of $\Delta\phi$: $u(\Delta\phi)$	1.51°	$\frac{\partial\kappa}{\partial(\Delta\phi)} = 0.30 \text{ W}\cdot\text{m}^{-1}\cdot\text{K}^{-1}\cdot\text{°}^{-1}$	0.45
Uncertainty of density: $u(\rho)$	44.6 kg·m ⁻³	$\frac{\partial\kappa}{\partial\rho} = 0.01 \text{ W}\cdot\text{m}^2\cdot\text{K}^{-1}\cdot\text{kg}^{-1}$	0.38
Uncertainty of heat capacity: $u(C_p)$	31.0 J·kg ⁻¹ ·K ⁻¹	$\frac{\partial\kappa}{\partial C_p} = 0.05 \text{ s}^{-1}\cdot\text{m}^{-1}\cdot\text{kg}^{-1}$	1.54
Combined standard uncertainty $u(\kappa)$			1.65
Expanded uncertainty $U = 2u(\kappa)$			3.30

$\kappa = 46.2 \text{ W}\cdot\text{m}^{-1}\cdot\text{K}^{-1}$ at 2215 K

Table 9 Uncertainty evaluation in thermal diffusivity at 2215 K

Component	Standard uncertainty	Sensitivity coefficient	Contribution (m ² ·s ⁻¹)
Uncertainty of function of thermal conductivity: $u(\kappa)$	1.65 W·m ⁻¹ ·K ⁻¹	$\frac{\partial\alpha}{\partial\kappa} = 1.98 \times 10^{-7} \text{ J}^{-1}\cdot\text{K}\cdot\text{m}^3$	3.21×10^{-7}
Uncertainty of density: $u(\rho)$	44.6 kg·m ⁻³	$\frac{\partial\alpha}{\partial\rho} = -1.68 \times 10^{-9} \text{ kg}^{-1}\cdot\text{s}^{-1}\cdot\text{m}^5$	-7.51×10^{-8}
Uncertainty of heat capacity: $u(C_p)$	31.0 J·kg ⁻¹ ·K ⁻¹	$\frac{\partial\alpha}{\partial C_p} = -9.87 \times 10^{-9} \text{ J}^{-1}\cdot\text{m}^2\cdot\text{kg}\cdot\text{K}\cdot\text{s}^{-1}$	-3.06×10^{-7}
Combined standard uncertainty $u(\alpha)$			4.54×10^{-7}
Expanded uncertainty $U = 2u(\alpha)$			9.08×10^{-7}

$\alpha = 0.91 \times 10^{-5} \text{ m}^2\cdot\text{s}^{-1}$ at 2215 K

by Itami and Shimoji [53] was used. Susa’s group [54, 55] described the spectral radiation mechanism, which involves of the excitation-relaxation of the free electrons and the inner shell electrons; the former being called an interband transition and the latter called an intraband transition. For transition metals and noble metals, the interband transition mainly occurs through the excitation of electrons from the *d* band to the conduction band above Fermi level, affecting ϵ in the visible region. In the Drude model, the intraband transition can be interpreted but the influence on the interband transition is not considered. As the wavelength decreases, the difference between the calculated and experimental emissivity increases. This indicates the effect of interband transition of electrons.

4.3 Wiedemann–Franz Law

The thermal conductivity (κ) is expressed as

Table 10 Values used to calculate normal spectral emissivity of V melts by the Drude model at melting point

Properties	Values
Density $\rho/\text{kg}\cdot\text{m}^{-1}$	5452
Electrical resistivity $\rho_{\text{el}}/\Omega\cdot\text{m}$	1.35×10^{-6} [24]
The number of free electrons per atom	1.49 [53]
Number of free electrons per unit volume/ m^{-3}	9.60×10^{28}
Plasma frequency/ $\text{rad}\cdot\text{s}^{-1}$	1.75×10^{16}
Relaxation time of free electrons/s	2.74×10^{-16}
Electron mass/kg	9.11×10^{-31}
Permittivity of the vacuum/ $\text{F}\cdot\text{m}^{-1}$	8.85×10^{-12}
Charge of the electron/C	1.60×10^{-19}
Emissivity at 600 nm obtained from Drude model	0.315
Emissivity at 807 nm obtained from Drude model	0.298
Emissivity at 940 nm obtained from Drude model	0.288
Emissivity at 1500 nm obtained from Drude model	0.255

$$\kappa = \kappa_{\text{vib}} + \kappa_{\text{el}}, \quad (21)$$

where κ_{vib} and κ_{el} denote the atomic thermal vibration part and the free electron contribution part in the thermal conductivity, respectively. According to the Wiedemann–Franz law, κ_{el} depends on the electrical resistivity (ρ_{el}) and Lorenz number ($L = 2.45 \times 10^{-8}/\text{W}\cdot\Omega\cdot\text{K}^{-2}$),

$$\kappa_{\text{el}} = LT\rho_{\text{el}}^{-1}. \quad (22)$$

From Figs. 10 and 11, the value obtained was larger than that reported by Pottlacher et al. [24] which were calculated using the Wiedemann–Franz law. The difference may have risen from the contribution of the thermal vibration of the atoms to the thermal conductivity of the V melt.

4.4 Correlation Between Density of States and Thermal Conductivity

In 1936, Mott [6, 7] reported the relationship between electrical current and the DOS at the Fermi level ($N(E_{\text{F}})$) of the transition metals; specifically.

1. The electrical current is carried by almost all the s electrons, each having an effective mass of approximately that of a free electron.
2. The electrical resistivity is mainly attributed to the s electron transition to the d state (i.e., s – d transition), and the conduction of the electrons in the d state is relatively smaller because of the heavier effective mass.
3. The probability of an s – d transition is proportional to the DOS in the d state.

These observations constitute Mott's s – d scattering model.

Based on the scattering model, our group found a linear correlation between the reciprocal DOS at the Fermi level $(N(E_F))^{-1}$ and α for six transition metals in liquid states [23].

With the additional V melt data, we were able to discuss further the correlation between $(N(E_F))^{-1}$ and thermophysical properties. Figure 12a plots $(N(E_F))^{-1}$ for liquid states of seven transition metals [23, 56]. Similarly, Fig. 12b plots the thermal conductivity (left vertical axis) and thermal diffusivity (right vertical axis) for these same transition metals.

For ease of comparison, their values of $(N(E_F))^{-1}$, α , and κ are listed in Table 11. The value in Table 11 represent data at a temperature ranging from -25 K to 50 K from the melting point of respective metals. Figure 12a and b shows the same trend in elemental dependence for $(N(E_F))^{-1}$ and α . Figure 12c shows for these transition metals near linearity in the dependence of $(N(E_F))^{-1}$ on α with one exception the Pd melt, which deviates from the trend because of a large contribution from thermal vibration of the atoms [23]. This result from V melts indicates that heat conduction in transition metals can be roughly explained with Mott's s - d scattering model, in which the s -electrons mainly carry the heat.

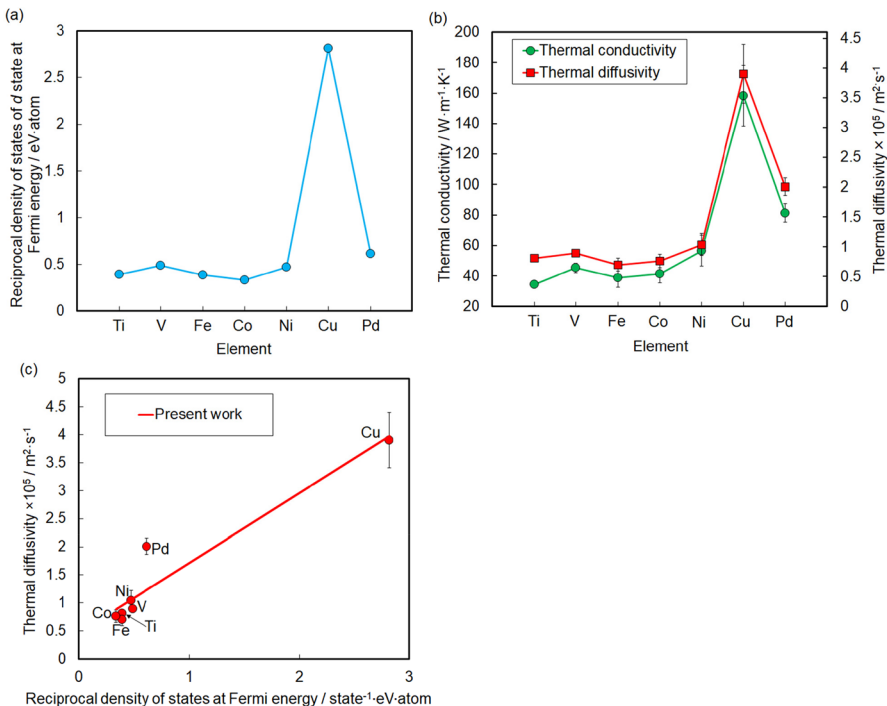


Fig. 12 (a) Reciprocal density of states at the Fermi level of transition metals in the liquid state [23, 56], (b) Thermal conductivity (left vertical axis) and thermal diffusivity (right vertical axis) of transition metals in the liquid state. (c) Correlation between the reciprocal density of states at the Fermi level and thermal diffusivity of transition metals. All error bars indicate expanded uncertainty ($k=2$)

Table 11 Reciprocal density of states at the Fermi level, thermal diffusivity, and thermal conductivity of transition metals in the liquid state

Element	Atomic number	Temperature/K	Reciprocal density of state at Fermi level: $(N(E_F))^{-1}/\text{state}^{-1}\text{eV}\cdot\text{atom}$	Thermal diffusivity: $\alpha/\text{m}^2\cdot\text{s}^{-1}$	Thermal conductivity: $\kappa/\text{W}\cdot\text{m}^{-1}\cdot\text{K}^{-1}$
V (Present work)	23	2200	0.49 [56]	8.95×10^{-6} [Present work]	45.3 [Present work]
Ti [23]	22	1973	0.39 [56]	8.08×10^{-6}	34.0
Fe [23]	26	1833	0.39	6.99×10^{-6}	38.7
Co [23]	27	1823	0.34	7.63×10^{-6}	41.4
Ni [23]	28	1773	0.47	10.4×10^{-6}	56.7
Cu [23]	29	1413	2.82	39.1×10^{-6}	158
Pd [23]	46	1823	0.61	20.0×10^{-6}	81.3

5 Conclusion

In this study, density, normal spectral emissivity between 807 nm and 940 nm, heat capacity at constant pressure, and thermal conductivity of the V melt were measured using the PROSPECT facility. The value obtained for the normal spectral emissivity of the V melt was larger than that calculated by the Drude model. This indicates that the effect of interband transitions of *d*-state electrons increases with decreasing wavelength. Likewise, the value obtained for the thermal conductivity was larger than that obtained from the Wiedemann–Franz law. The difference between the two reflects the contribution to thermal conduction from the thermal vibration of atoms in the melt. The thermal diffusivity of the V melt was determined from the density, heat capacity, and thermal conductivity. The value obtained is approximately proportional to the reciprocal DOS at the Fermi level, and likewise for other transition metals. Except for the Pd melt, the thermal diffusivities of the transition elements in the liquid state can be explained by Mott's *s*–*d* scattering model and the heat of the transition elements is transported by *s*-electrons.

Acknowledgements We thank Richard Haase, PhD, from Edanz (<https://jp.edanz.com/ac>) for editing a draft of this manuscript.

Author Contributions M.W. wrote the main manuscript. M.A. and H. F. reviewed and revised the manuscript.

Funding This work was supported by Japan Society for the Promotion of Science (JSPS) KAKENHI Grants 20K22464 and 21K14447.

Data Availability No datasets were generated or analysed during the current study.

Declarations

Competing interests The authors declare no competing interests.

Open Access This article is licensed under a Creative Commons Attribution 4.0 International License, which permits use, sharing, adaptation, distribution and reproduction in any medium or format, as long as you give appropriate credit to the original author(s) and the source, provide a link to the Creative Commons licence, and indicate if changes were made. The images or other third party material in this article are included in the article's Creative Commons licence, unless indicated otherwise in a credit line to the material. If material is not included in the article's Creative Commons licence and your intended use is not permitted by statutory regulation or exceeds the permitted use, you will need to obtain permission directly from the copyright holder. To view a copy of this licence, visit <http://creativecommons.org/licenses/by/4.0/>.

References

1. J.B.V. Zytveld, Electrical resistivity of liquid chromium. *J. Non-Cryst. Solid*, **61 and 62**, 1085–1090 (1984)
2. H. Ikeda, F. Salleh, Influence of heavy doping on Seebeck coefficient in silicon-on-insulator. *Appl. Phys. Lett.* **96**, 012106 (2009)

3. B. Hinterleitner, F. Garmroudi, N. Reumann, T. Mori, E. Bauer, R. Podloucky, The electronic pseudo band gap states and electronic transport of the full-Heusler compounds Fe₂Val. *J. Mater. Chem. C* **9**, 2073–2085 (2021)
4. H. Miyazaki, S. Tateishi, M. Matsunami, K. Suda, S. Yamada, K. Hamaya, Y. Nishino, Direct observation of pseudo-gap electronic structure in the Heusler-type Fe₂Val thin film. *J. Electron. Spectrosc. Relat. Phenom.* **232**, 1–4 (2019)
5. T. Aisaka, M. Shimizu, Electrical resistance, Thermal conductivity and Thermoelectric power of transition metals at high temperatures. *J. Phys. Soc. Jpn.* **28**, 646–654 (1970)
6. N.F. Mott, The electrical conductivity of transition metals. *Proc. R. Soc. A* **153**, 699–717 (1936)
7. N.F. Mott, The resistance and thermoelectric properties of the transition metals. *Proc. R. Soc. A* **156**, 368–382 (1936)
8. U. Mizutani, *Introduction to the Electron Theory of Metals* (Cambridge University Press, Cambridge, 2001)
9. VYe. Zinov'yev, V.F. Polev, S.G. Taluts, G.P. Zinov'yeva, S.A. Il'inykh, Diffusivity and thermal conductivity of 3d-transition metals in solid and liquid states. *Phys. Met. Metallogr.* **61**, 85–92 (1986)
10. M.J. Assael, A. Chatzimichailidis, K.D. Antoniadis, W.A. Wakeham, M.L. Huber, H. Fukuyama, Reference correlations for the thermal conductivity of liquid copper, gallium, indium, iron, lead, nickel and tin. *High Temp. High Press.* **46**, 391–416 (2017)
11. M. Watanabe, M. Adachi, H. Fukuyama, Densities of Fe–Ni melts and thermodynamic correlations. *J. Mater. Sci.* **51**, 3303–3310 (2016)
12. H. Fukuyama, M. Watanabe, M. Adachi, Recent studies on thermophysical properties of metallic alloys with PROSPECT: excess properties to construct a solution model. *High Temp. High Press.* **49**, 197–210 (2019)
13. M. Watanabe, M. Adachi, H. Fukuyama, Density measurement of Ti–X (X = Cu, Ni) melts and thermodynamic correlations. *J. Mater. Sci.* **54**, 4306–4313 (2019)
14. M. Adachi, Y. Yamagata, M. Watanabe, S. Hamaya, M. Ohtsuka, H. Fukuyama, Composition dependence of normal spectral emissivity of liquid Ni–Al alloys. *ISIJ Int.* **61**, 684–689 (2021)
15. H. Fukuyama, H. Higashi, H. Yamano, Effect of B4C addition on the solidus and liquidus temperature, density and surface tension of type 316 austenitic stainless steel in the liquid state. *J. Nucl. Mater.* **554**, 153100 (2021)
16. M. Watanabe, M. Adachi, H. Fukuyama, Densities of Au–X (X = Cu, Ni and Pd) binary melts and thermodynamics correlations. *J. Mol. Liq.* **348**, 118050 (2021)
17. M. Watanabe, Y. Takahashi, S. Imaizumi, Y. Zhao, M. Adachi, M. Ohtsuka, A. Chiba, Y. Koizumi, H. Fukuyama, Thermophysical properties of liquid Co–Cr–Mo alloys measured by electromagnetic levitation in a static magnetic field. *Thermochim. Acta* **708**, 179119 (2022)
18. T. Tsukada, H. Fukuyama, H. Kobatake, Determination of thermal conductivity and emissivity of electromagnetically levitated high-temperature droplet based on the periodic laser-heating method: Theory. *Int. J. Heat Mass Transf.* **50**, 3054–3061 (2007)
19. M. Watanabe, M. Adachi, M. Uchikoshi, H. Fukuyama, Thermal conductivities of Fe–Ni melts measured by non-contact laser modulation calorimetry. *Metall. Mater. Trans. A* **50**, 3295–3300 (2019)
20. M. Watanabe, M. Adachi, H. Fukuyama, Correlation between excess volume and thermodynamic functions of liquid Pd–X (X = Fe, Cu and Ni) systems. *J. Chem. Thermodyn.* **130**, 9–16 (2019)
21. M. Watanabe, J. Takano, M. Adachi, M. Uchikoshi, H. Fukuyama, Thermophysical properties of liquid Co measured by electromagnetic levitation technique in a static magnetic field. *J. Chem. Thermodyn.* **121**, 145–152 (2018)
22. M. Watanabe, M. Adachi, H. Fukuyama, Normal spectral emissivity and heat capacity at constant pressure of Fe–Ni melts. *J. Mater. Sci.* **52**, 9850–9858 (2017)
23. M. Watanabe, M. Adachi, H. Fukuyama, Heat capacities and thermal conductivities of palladium and titanium melts and correlation between thermal diffusivity and density of states for transition metals in a liquid state. *J. Mol. Liq.* **324**, 115138 (2021)
24. G. Potlacher, T. Hüpf, B. Wilthan, C. Cagran, Thermophysical data of liquid vanadium. *Thermochim. Acta* **461**, 88–95 (2007)
25. J.F. Smith, The Fe–V (iron–vanadium) system. *Bull. Alloy Phase Diag.* **5**, 184–194 (1984)
26. T. Saito, Y. Shiraiishi, Y. Sakuma, Density measurement of molten metals by levitation technique at temperatures between 1800 and 2200 degree. *Trans. Iron Steel Inst. Jpn.* **9**, 118–126 (1969)

27. P.F. Paradis, T. Ishikawa, T. Aoyama, S. Yoda, Thermophysical properties of vanadium at high temperature measured with an electrostatic levitation furnace. *J. Chem. Thermodyn.* **34**, 1929–1942 (2002)
28. V.P. Elyutin, V.I. Kostikov, I.A. Pen'kov, Effect of carbon on the surface tension and density of liquid vanadium, niobium, and molybdenum. *Sov. Powder Metall. Met. Ceram.* **9**, 37–41 (1970)
29. Y.N. Ivashchenko, P.S. Martsenyuk, Apparatus for measuring the surface energy and density of molten refractory metals. *Teplofiz. Vys. Temp.* **11**, 1285–1287 (1973)
30. M.A. Maurakh, Surface tension of titanium, zirconium and vanadium. *Trans. Indian Inst. Met.* **14**, 209–225 (1964)
31. B. Reiplinger, J. Brillo, Density and excess volume of the liquid Ti–V system measured in electromagnetic levitation. *J. Mater. Sci.* **57**, 7954–7964 (2022)
32. C.H. Zhang, P.F. Zou, L. Hu, H.P. Wang, B. Wei, Composition dependence of thermophysical properties for liquid Zr–V alloys determined at electrostatic levitation state. *J. Appl. Phys.* **131**, 165104 (2022)
33. R. Lin, M.G. Froberg, Enthalpy measurements on solid and liquid vanadium by levitation calorimetry/Enthalpiemessungen an festem und flüssigem Vanadium mit dem Schwebeschmelz-Dropkalorimeter. *Int. J. Mater. Res.* **82**, 48–52 (1991)
34. J.A. Treverton, J.L. Margrave, Thermodynamic properties by levitation calorimetry III. The enthalpies of fusion and heat capacities for the liquid phases of iron, titanium, and vanadium. *J. Chem. Thermodyn.* **3**, 473–481 (1971)
35. J.L. McClure, A. Cezairliyan, Radiance temperatures (in the wavelength range 525 to 906 nm) of vanadium at its melting point by a pulse-heating technique. *Int. J. Thermophys.* **18**, 291–302 (1997)
36. A. Cezairliyan, A.P. Miller, F. Righini, A. Rosso, Radiance temperature of vanadium at its melting point. *High Temp. Sci.* **11**, 223–232 (1979)
37. C. Ronchi, J.P. Hiernaut, G.J. Hyland, Emissivity X points in Solid and liquid refractory transition metals. *Metrologia* **29**, 261–271 (1992)
38. B.Y. Berezin, S.A. Kats, V.Y. Chekhovskoi, Spectral emissivities of molten refractory metals. *Teplofiz. Vys. Temp.* **14**, 497–502 (1976)
39. T. Ishikawa, C. Koyama, Y. Nakata, Y. Watanabe, P.F. Paradis, Spectral emissivity, hemispherical total emissivity, and constant pressure heat capacity of liquid vanadium measured by an electrostatic levitator. *J. Chem. Thermodyn.* **163**, 106598 (2021)
40. B.Y. Berezin, V.Y. Chekhovskoi, A.E. Sheindlin, Heat of fusion of vanadium. *Sov. Phys. Dokl.* **16**, 1007–1009 (1972)
41. K. Schaefer, M. Rösner-Kuhn, M.G. Froberg, Enthalpy measurements of undercooled melts by levitation calorimetry: the pure metals nickel, iron, vanadium and niobium. *Mater. Sci. Eng. A* **197**, 83–90 (1995)
42. J.W. Arblaster, Thermodynamic properties of vanadium. *J. Phase Equilib. Diffus.* **38**, 51–64 (2015)
43. M.W. Chase, *NIST-JANAF Thermochemical Tables*, 4th edn. (American Chemical Society, Washington, 1998)
44. B.Y. Berezin, V.Y. Chekhovskoy, A.E. Sheindlin, The enthalpy and specific heat of molten vanadium. *High Temp. Sci.* **4**, 478–486 (1972)
45. P.D. Desai, Thermodynamic properties of vanadium. *Int. J. Thermophys.* **7**, 213–228 (1986)
46. R. Hultgren, P.D. Desai, D.T. Hawkins, M. Gleiser, K.K. Kelley, *Selected Values of the Thermodynamic Properties of the Elements* (American Society for Metals, Metals Park, 1973)
47. R. Hultgren, R.L. Orr, P.D. Anderson, K.K. Kelley, *Selected Values of Thermodynamics Properties of Metals and Alloys* (Wiley, New York, 1963)
48. A.T. Dinsdale, SGTE data for pure elements. *CALPHAD* **15**, 317–425 (1991)
49. Y. Sun, H. Muta, Y. Ohishi, Heat capacity of liquid transition metals obtained with aerodynamic levitation. *J. Chem. Thermodyn.* **171**, 106801 (2021)
50. V.E. Zinov'yev, V.F. Polev, S.G. Taluts, P.V. Gel'd, Anomalies of the thermal diffusivity and thermal conductivity of vanadium, niobium, and tantalum near their melting points. *Sov. Phys. Solid State* **28**, 1639–1640 (1986)
51. K.C. Mills, B.J. Monaghan, B.J. Keene, Thermal conductivities of molten metals: Part 1, pure metal. *Int. Mater. Rev.* **41**, 209–242 (1996)
52. JCGM 100:2008, Evaluation of measurement data—guide to the expression of uncertainty in measurement. Joint Committee for Guides in Metrology (2008)
53. T. Itami, M. Shimoji, Application of simple model theories to thermodynamic properties of liquid transition metals. *J. Phys. F Met. Phys.* **14**, L15–L20 (1985)

54. R. Tanaka, T. Sato, M. Susa, Temperature and compositional dependencies of normal spectral emissivities at 6328 nm for solid Cu–Ni alloys—ellipsometric measurements and formulation of empirical prediction equation. *Metall. Mater. Trans. A* **36A**, 1507–1514 (2005)
55. H. Watanabe, M. Susa, H. Fukuyama, K. Nagata, Near-infrared spectral emissivity of Cu, Ag, and Au in the liquid and solid states at their melting points. *Int. J. Thermophys.* **24**, 1105–1120 (2003)
56. L.D. Phuong, A. Pasturel, D.N. Manh, Effect of s-d hybridization on interatomic pair potentials of the 3d liquid transition metals. *J. Phys. Condens. Matter* **5**, 1901–1918 (1993)

Publisher's Note Springer Nature remains neutral with regard to jurisdictional claims in published maps and institutional affiliations.